Nano Res (2009) 2: 406–415
DOI 10.1007/s12274-009-9040-9
Research Article

# PtAu Bimetallic Heteronanostructures Made by Post-Synthesis Modification of Pt-on-Au Nanoparticles

Zhenmeng Peng and Hong Yang (✉)

Department of Chemical Engineering, University of Rochester, Gavett Hall 206, Rochester, NY 14627, USA

Received: 22 January 2009 / Revised: 10 March 2009 / Accepted: 16 March 2009


## ABSTRACT

Bimetallic PtAu heteronanostructures have been synthesized from Pt-on-Au nanoparticles, which were made from platinum acetylacetonate and gold nanoparticles. Using the Pt-on-Au nanoparticles as precursors, Pt-surface rich PtAu bimetallic heteronanostructures can be produced through controlled thermal treatments, as confirmed by field emission high-resolution transmission electron microscopy (HR-TEM) and elemental mapping using a high-angle annular dark-field scanning transmission electron microscope (HAADF-STEM). Oxidation of formic acid was used as a model reaction to demonstrate the effects of varying composition and surface structure on the catalytic performance of PtAu bimetallic nanostructures. Cyclic voltammetry (CV) showed that these carbon-supported PtAu heteronanostructures were much more active than platinum in catalyzing the oxidation of formic acid, judging by the mass current density. The results showed that post-synthesis modification can be a very useful approach to the control of composition distributions in alloy nanostructures.

## KEYWORDS

Nanostructure, alloy, platinum, gold, formic acid oxidation, electrocatalyst, polymer electrolyte membrane fuel cell (PEMFC)

## Introduction

Metal alloys, in particular those containing platinum, have attracted considerable attention in recent years because of the increasing demand for high performance catalysts in fuel cells and other applications [1–9]. It has been shown that a $Pt_3Ni$ (111) surface is much more active than the corresponding Pt (111) surface in the oxygen reduction reaction (ORR), and over 90 times more active than the state-of-the-art carbon-supported platinum (Pt/C) catalysts [4]. The dramatic enhancement is associated with the surface electronic and geometric structures of the platinum atoms in the former species [3, 4, 10]. Thus in order to make highly active catalysts, the surface compositions of nanoalloys need to be engineered synergistically [1, 2, 11, 12]. Post-synthesis modification of alloys has emerged as a viable approach to address the challenges of controlling the location of different metal elements in nanostructures. Under tailored reactive environments, surface structures and compositions

Address correspondence to hongyang@che.rochester.edu

of $Rh_{50}Pd_{50}$ were tuned by using NO, CO, and other gases [11], demonstrating that high levels of control can be achieved for such metal alloys.

In this work we focus on the design and synthesis of Pt-surface rich PtAu bimetallic nanostructures from Pt-on-Au nanoparticles. We and others have previously demonstrated that the sequential synthesis of core-shell nanoparticles from molecular precursors is readily achievable [13, 14], as heterogeneous nucleation and growth are often favored thermodynamically [15]. The advantage of the sequential method is its ability to deposit one component at a time. The as-made core-shell nanoparticles can be converted to new compositions on solid supports at relatively mild temperatures [14]. Heterogeneity in composition should be attainable by carefully controlling the reaction conditions, because solid state diffusion is typically slow near room temperature. Such multifunctional heterogeneous alloy nanostructures may potentially be used as highly active and low platinum content electrocatalysts [1, 16, 17] which is a critical area for the development of polymer electrolyte membrane fuel cells (PEMFCs), a major class of low-temperature energy conversion devices using small molecules as fuels [18, 19].

Effects of the formation of alloys on the electrocatalytic properties of platinum are studied using direct oxidation of formic acid as a model reaction. This fuel has several advantages over other small molecules commonly used for PEMFCs [19–23]. A direct formic acid fuel cell (DFAFC) has a fairly high theoretical open circuit voltage (1.45 V) and experiences fewer problems in fuel crossover than a direct methanol fuel cell (DMFC) [24, 25]. The kinetics of chemical oxidation of formic acid are sensitive to changes in the surface structure and composition of the electrocatalysts. It is known that this oxidation can involve both dehydrogenation and dehydration, which are described by the following two reactions [18, 21, 26]:

$$HCOOH \xrightarrow{\text{dehydrogenation}} CO_2 + 2H^+ + 2e^- \quad (1)$$

$$HCOOH \xrightarrow{\text{dehydration}} CO_{ads} + H_2O \rightarrow CO_2 + 2H^+ + 2e^- \quad (2)$$

In the dehydrogenation pathway, formic acid is completely oxidized to $CO_2$ in a single step on a catalyst, typically made of carbon-supported platinum nanoparticles. In contrast, in the dehydration pathway, formic acid first generates CO-like intermediates ($CO_{ads}$) on the catalytic surfaces. These intermediates are then oxidized electrochemically to produce $CO_2$. In the latter reaction pathway, the absorbed CO intermediates can block the active sites and slow down the overall reaction. Dehydrogenation is the main pathway in the low potential range between 0.2 and 0.7 V, although adsorbed $CO_{ads}$ can still be generated via dehydration [18, 20, 21]. The coverage of Pt active sites by $CO_{ads}$ species increases with the potential, resulting in the loss of available active sites. The CO poisoning can by greatly suppressed by using bimetallic platinum electrocatalysts. It has been shown that both PtPb and PtBi intermetallics can have higher activities than pure platinum metal in catalyzing this oxidation reaction [27–30]. The improved adsorption of formic acid has been attributed to electronic effects, while the reduced poisoning by $CO_{ads}$ is because of geometric effects [31–33]. High performance in the oxidation of formic acid has been observed for both PtAu alloy nanoparticles [25, 34] and Pt-modified Au nanoparticles [5, 35, 36].

## 1. Experimental

**Synthesis of gold nanoparticles.** Oleylamine-stabilized gold nanoparticles were prepared using a modified Brust–Schiffrin method [37, 38]. A solution of tetraoctylammonium bromide (TOAB, 98%, Aldrich, 0.73 g, 1.3 mmol) in toluene (99.8%, Aldrich, 26.7 mL) was mixed with 10 mL of an aqueous solution of gold (III) chloride trihydrate ($HAuCl_4 \cdot 3H_2O$, >99.9%, Aldrich, 0.06 g, 0.15 mmol) in a 100-mL flask. This two-phase mixture was vigorously stirred using a mechanical stirrer (VWR Scientific) until all the tetrachloroaurate ions were transferred into the toluene phase. A freshly-made aqueous solution (8.3 mL) of sodium borohydride (99%, Aldrich, 0.13 g , 3.3 mmol) was slowly added into the toluene phase over 10 min with vigorous stirring. After reaction for additional 1 h, oleylamine (70%, Aldrich, 0.88 mL) was added to the toluene

phase. The particles dispersed in toluene were separated out from the reaction mixtures and mixed with 50 mL of ethanol. The nanoparticle product was precipitated out by centrifugation at 6000 rpm for 5 min (Beckman Coulter, Allegra™ 21 centrifuge). This precipitate was washed with 7.5 mL of chloroform and 22.5 mL of ethanol, followed by centrifugation at 6000 rpm for 5 min. The as-made gold nanoparticles were dispersed in 5 mL of diphenyl ether (DPE, 99%, Aldrich) for further use.

**Synthesis of Pt-on-Au nanoparticles.** In a typical procedure, oleylamine (0.3 mL, 0.9 mmol) was added to a solution of platinum acetylacetonate ($Pt(acac)_2$, 98%, Strem, 0.02 g, 50 μmol) in DPE (4 mL), followed by the addition of a dispersion of gold nanoparticles (12.5 μmol) in DPE (1 mL). The number of moles of gold was calculated based on the amount of metal determined by the thermal gravimetric analysis (TGA) technique using air as carrier gas. The total volume of DPE was fixed at 5 mL for all experiments. The reaction was conducted at 180 °C under argon for 1 h, unless stated otherwise. The product was precipitated out from the mixture by adding 10 mL of ethanol as the antisolvent, followed by centrifugation at 6000 rpm for 10 min. The precipitate was collected and dispersed in 2 mL of hexane. The ratio of these two metal precursors, reaction temperature and time were varied systematically to study the effect on the formation of Pt-on-Au nanostructures. To study the effect of feed ratio, we adjusted the amount of gold nanoparticles while all other variables were kept unchanged. The Pt/Au atomic ratio in the reaction mixture was changed from one to six by adding different amounts of $Pt(acac)_2$ and Au nanoparticles.

**Preparation of PtAu bimetallic heteronanostructures.** A suspension of 50 mg of carbon black (Vulcan XC-72) in 15 mL of hexane was sonicated at ambient room temperature for 1 h using a sonicator (Brandson, Model 2510), followed by the addition of 10 mg of Pt-on-Au nanoparticles. The total amount of metal in the nanoparticles was determined by TGA using air as carrier gas to a maximum temperature set at 800 °C. This mixture was stirred at room temperature overnight using a magnetic stirrer and precipitated out via centrifugation at 5000 rpm for 5 min. The resultant powder was thermally treated at 300 °C for 1 h in air at a ramping rate of 2 °C/min and then at 400 °C for 2 h in a forming gas of 5 vol% hydrogen in argon in a tube furnace (Lindberg/Blue, Mini-Lite tube furnace). The ramping rate was 1 °C/min for the segment between 300 and 400 °C.

**Characterization.** Transmission electron microscopy (TEM) images were recorded on a JEOL JEM 2000EX microscope at an accelerating voltage of 200 kV. High-resolution transmission electron microscopy (HR-TEM) images were obtained using a FEI Tecnai F20 microscope operated at 200 kV. Scanning transmission electron microscopy (STEM) images and elemental maps were obtained under high-angle angle annular dark field (HAADF) mode. Powder X-ray diffraction (PXRD) patterns were recorded using a Philips MPD diffractometer with a Cu Kα X-ray source having a wavelength of 1. 5405 Å. The PXRD patterns were fitted using a Gaussian function imbedded in Origin (OriginLab Corporation). Ultraviolet–visible (UV–vis) spectra were obtained with a UV/VIS/NIR spectrometer (Perkin–Elmer Lambda 900). The specimens used for UV–vis measurements were dispersions of nanoparticles in toluene. Energy dispersive X-ray (EDX) analysis was carried out on a field emission scanning electron microscope (FE-SEM, Zeiss-Leo DSM982). TGA was conducted on an SDT-Q600 system from TA Instruments.

Electrochemical properties were studied on a CHI 760 dual channel electrochemical workstation (CH Instruments, Inc.) using a three-electrode system that consisted of a glassy carbon working electrode (5 mm in diameter), a platinum wire counter electrode, and a hydrogen reference electrode (HydroFlex, Gaskatel). The ink of carbon-supported catalysts was prepared by dispersing in a mixture of deionized water, iso-propanol and 5 wt% Nafion® solution ($V_{water}:V_{2\text{-propanol}}:V_{5\%\ Nafion}=0.8:0.2:0.005$), followed by sonication at ambient room temperature for 10 min. The catalyst ink, which contained 1 μg of PtAu metals, was drop-cast onto the glassy carbon electrode and dried under a gentle stream of air. The amount of metals in a catalyst was quantified by TGA. For comparison, carbon-supported platinum (60 wt% Pt, E-TEK) and gold (20 wt%, E-TEK) catalysts were prepared according to the same protocol. The total amount of the catalyst was kept

at 1 μg of metals for all the tests. For electrochemical surface area (ECSA) measurements, 0.5 mol/L sulfuric acid ($H_2SO_4$) was used as the supporting electrolyte. For electrocatalytic oxidation of formic acid, the electrolyte was an aqueous solution of 0.5 mol/L $H_2SO_4$ and 0.5 mol/L formic acid. Before each measurement, the solution was bubbled with argon for 30 min to remove dissolved oxygen gas. For CO stripping experiments, the electrodes were pretreated by immersing in a CO-saturated 0.1 mol/L $HClO_4$ aqueous solution and held at 0.25 V for 20 min before the measurements. The CVs were typically run at the ambient room temperatures using a scan rate of 50 mV/s, unless stated otherwise.

## 2. Results and discussion

Figure 1 shows TEM images, elemental maps, and PXRD patterns of Pt-on-Au nanoparticles, and a representative TEM image of the gold nanoparticles used in the synthesis. The gold nanoparticles, which were made using the Brust–Schiffrin method [37, 38], had an average diameter of 7.4 nm ± 1.0 nm (Fig. 1(a)). The PXRD pattern of these nanoparticles showed five diffraction peaks that can be indexed to (111), (200), (220), (311), and (222) planes of face-centered cubic (fcc) gold metal. Upon the addition of $Pt(acac)_2$, secondary particles formed on the surface of Au cores could be clearly observed by TEM after reaction for 1 h at 180 °C (Fig. 1(b)). The formation of platinum-on-gold nanoparticles most likely involved either island or island-on-wetting layer growth. EDX analysis indicated that these nanoparticles contained both Pt and Au elements and had an average Pt/Au atomic ratio of 0.63 (Fig. S-1 in the Electronic Supplementary Material (ESM)). The distributions of these two metal elements in the nanoparticles were investigated by EDX using STEM mode. Figures 1(c)–(e) shows the STEM image of an individual Pt-on-Au nanoparticle and its corresponding elemental maps for Pt and Au. Both Au and Pt metals were readily detectable, though their distributions within the particle were quite different. While Au could only be found in the core region, with a size much smaller than that of the nanoparticle (Fig. 1(c)), platinum was distributed throughout the entire particle including the branches that were outside the core. HR-TEM showed that these nanoparticles were crystalline, judging by the well-defined fringes (Fig. 1(f)). The labeled lattices could be indexed to the (200) crystal plane of fcc platinum metal. These observations suggest that the nanoparticles were composed of gold cores and platinum branches. No obvious grain boundaries between the branches and cores could be observed, and the heterogeneous nucleation and growth most likely followed either Stranski–Krastanov (SK) or Volmer–Weber (VW) modes [39]. The growth of heterogeneous nanostructures should be favored thermodynamically [40], as the lattice mismatch between gold and platinum metals is only about 4% and the strain energy for heterogeneous nucleation is small in such a case because of a gradual relaxation of platinum lattices at the interfaces between Au and Pt [41]. The PXRD pattern (Fig. 1(g)) shows that the diffraction patterns for these nanoparticles could be

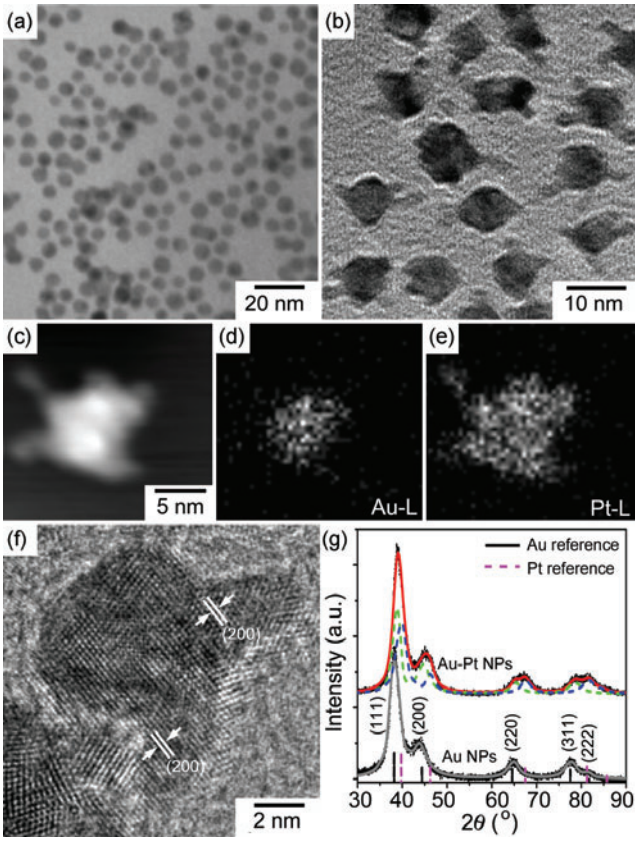


**Figure 1** Representative TEM images of (a) Au and (b) Pt-on-Au nanoparticles, (c) STEM and (d), (e) EDX maps of Au and Pt elements, and (f) HRTEM image of a single Pt-on-Au nanoparticle, and (g) the corresponding XRD patterns of the Au and Pt-on-Au nanoparticles. All Pt-on-Au nanoparticles were made at 180 °C for 1 h

deconvoluted very well into two sets of diffraction peaks for pure gold and pure platinum.

The growth of platinum on gold nanoparticles was followed by UV–vis spectroscopy and TEM studies (Fig. 2). The plasmon resonance band in the visible range arising from gold nanoparticles is sensitive to changes in the surface and has been used to study the process of coating by inorganic materials [37, 42]. Figure 2 shows representative UV–vis spectra and the corresponding TEM images of Au and Pt-on-Au nanoparticles obtained at a series of reaction points. The gold particles showed the characteristic plasmon resonance band at around 510 nm [37, 43, 44]. This absorbance became smaller for the Pt-on-Au nanoparticles over time, and disappeared almost completely for the particles formed after reaction for 60 min. No absorbance peak was observed for those Pt-on-Au nanoparticles formed after reaction for 120 min. The UV–vis spectroscopic data agreed well with the TEM observation (Fig. 2). The evolution of branches on the cores could clearly be observed. Fairly large and multilayered particle-on-particle morphology was observed for those formed after reaction for 120 min.

Besides reaction time, the overall morphology and size of Pt-on-Au nanoparticles could also be controlled by varying the reaction temperature (Fig. 3). For an Au nanoparticle/$Pt(acac)_2$ feed ratio of 1:4 and with a reaction time of 1 h, increase in reaction temperature resulted in growth of large branches. The surface coverage of nanoparticles also increased and the optimal temperature range was found to be between 180 and 190 °C (Fig. 3). For those Pt-on-Au nanoparticles made at 170 °C, the platinum particles on Au surfaces were small, while those made at 200 °C tended to grow much larger. Similarly, the Au nanoparticle/$Pt(acac)_2$ feed ratio also affected the morphology of the branches and surface coverage of Pt-on-Au nanoparticles (Fig. S-2 in the ESM).

These Pt-on-Au nanoparticles provide an excellent platform to study the controlled synthesis of heterogeneous PtAu alloy nanostructures, since thermal properties of metal nanoparticles scale with size. In this study, carbon was used as the support to minimize the sintering of alloy nanoparticles. The carbon-supported Pt-on-Au nanoparticles were thermally treated first in air at 300 °C and then in forming gas (5 vol% hydrogen in argon) at 400 °C. The treatment at 300 °C in air was to facilitate the removal of surface capping agents through calcination. Figure 4 shows representative (S)TEM images, elemental maps, and PXRD pattern of carbon-supported Pt-on-Au nanoparticles and the corresponding PtAu alloy nanostructures obtained after the thermal treatment. The TEM image shows that the Pt-on-

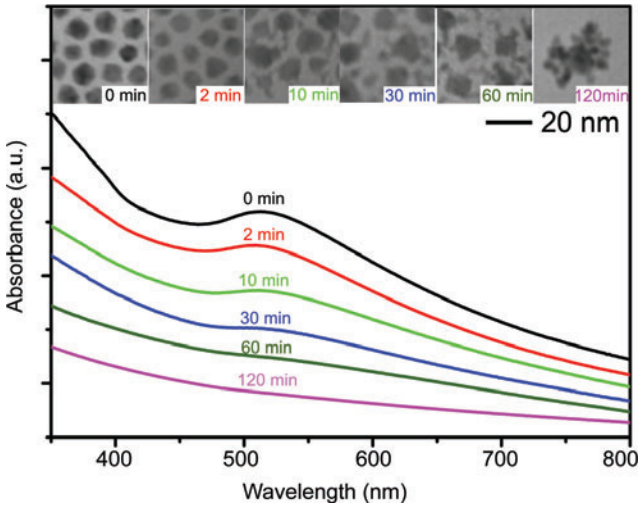


**Figure 2** UV–vis spectra and TEM images (insets) of Au (0 min) and Pt-on-Au nanoparticles made after different reaction times. The Au/Pt precursor feed ratio was 1:4 and the reaction temperature was 180 °C

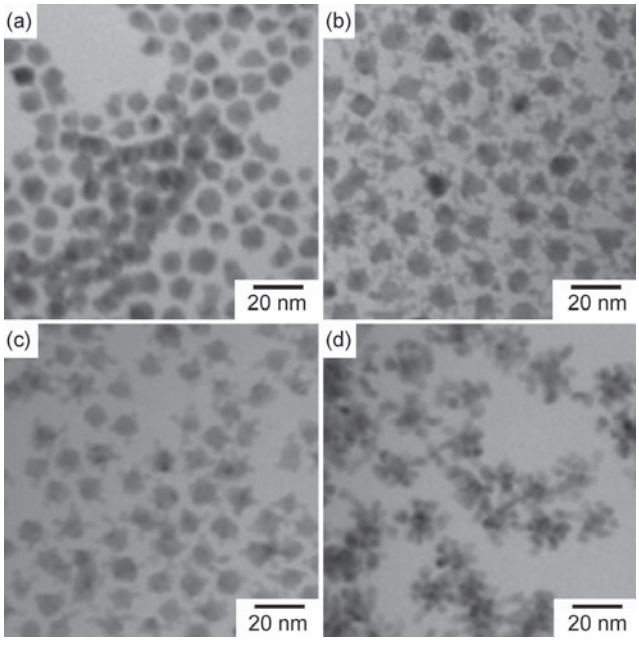


**Figure 3** TEM images of Pt-on-Au nanoparticles formed at four different reaction temperatures: (a) 170, (b) 180, (c) 190, and (d) 200 °C. The Au nanoparticle/$Pt(acac)_2$ feed ratio was 1:4 and the reaction time was 1 h

Au nanoparticles were well dispersed on the carbon supports (Fig. 4(a)). After the thermal treatment, the particles remained evenly distributed. While the overall size of the bimetallic particles did not seem to change dramatically, their surfaces became much smoother than those before the treatment (Fig. 4(b)). HR-TEM showed that the PtAu nanostructure was highly crystalline and possessed multiple domains (Fig. 4(c)). STEM images and elemental maps for Au and Pt indicate that Au was still distributed mainly in the core area, while Pt could be detected throughout the entire PtAu nanoparticle with relatively strong signals at the outer regions (Figs. 4(d)–(f)). Some Au signals could be detected in localized regions outside of the core, suggesting Au atoms diffused into the surface layers of Pt particles upon annealing at 400 °C. These findings suggest that an alloy of Pt and Au formed during the thermal treatment resulting in PtAu alloy nanostructures with surfaces rich in Pt. The PXRD pattern provides additional evidence that heterogeneity in PtAu alloy phases existed in these annealed nanoparticles (Fig. 4(g)). After the thermal treatment, the diffraction pattern split into two distinctive sets, which were in between those for pure Au and Pt metals. The separation became obvious for those peaks at high $2\theta$ angles. These two sets of diffraction peaks could be assigned to Au- and Pt-rich PtAu alloys (Fig. 4(g)). The compositions of these two alloys were estimated to be $Pt_{21}Au_{79}$ and $Pt_{81}Au_{19}$, respectively, based on the shift of peak positions and Vegard's law [45, 46]. As the overall Pt/Au atomic ratio was 0.63, the bimetallic nanostructures should therefore consist of about 70 % of $Pt_{21}Au_{79}$ and 30% of $Pt_{81}Au_{19}$ alloys. While they do not form a good solid solution and have a large miscibility gap in their bulk phase diagram, platinum and gold metals can form alloys at the nanometer scale at relatively low temperature [25, 34]. Similar phase behavior has also been observed in PtAg alloy nanostructures made from molecular precursors [46, 47]. It has been proposed that surface energy could be the main driving force for the formation of these nanoalloys [48]. The PXRD pattern also showed that the crystallinity of these bimetallic nanostructures (PtAu/C) improved substantially as the diffraction peaks became sharper than those for Pt-on-Au nanoparticles.

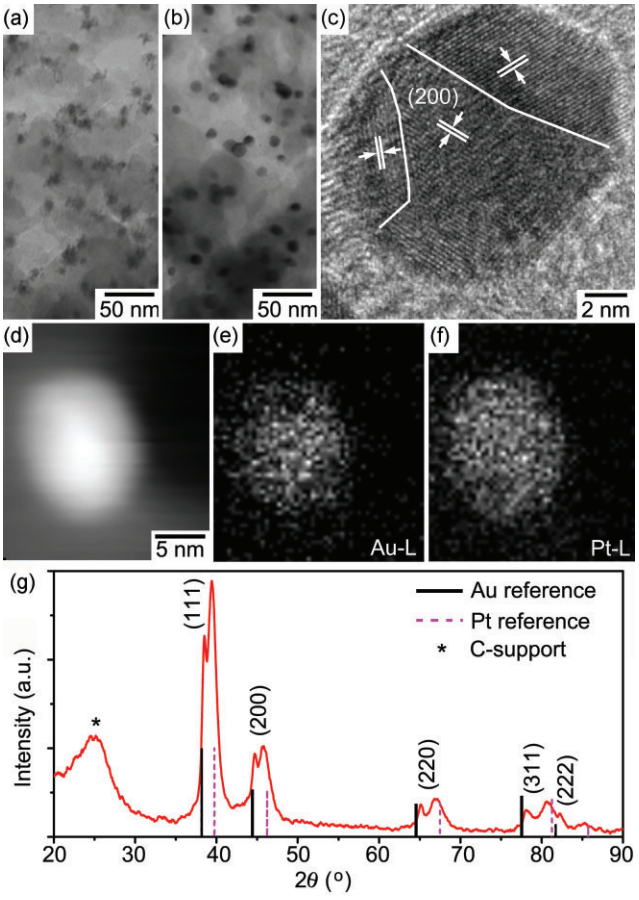


**Figure 4** Representative TEM images of Pt-on-Au nanoparticles on carbon supports (a) before and (b) after thermal treatment; (c) HR-TEM image; (d) STEM image; ((e), (f)) the corresponding the elemental maps for Au and Pt metals; (g) PXRD pattern of PtAu alloy heteronanostructures obtained by thermal treatment

Figure 5 shows the CV curves for the oxidation of formic acid using PtAu/C as the electrocatalysts. Commercial carbon-supported Pt (Pt/C, 60 wt% Pt E-TEK) and Au (Au/C, 20 wt%, E-TEK) catalysts were tested for comparison. The average size and size distribution of these two commercial catalysts determined by TEM were 3.5 nm ± 0.7 nm for Pt/C and 7.6 nm ± 3.1 nm for Au/C (Fig. S-3 in the ESM). The current density was normalized according to the unit mass of metals rather than ECSA, because the conventional method for determining ECSA is based on hydrogen adsorption/desorption [49, 50]. Since gold metal does not show measurable hydrogen adsorption, such electrochemical methods cannot be used to measure the true surface areas of PtAu alloys (Fig. S-4 in the SEM). The mass current density is also the preferred measure for practical applications.

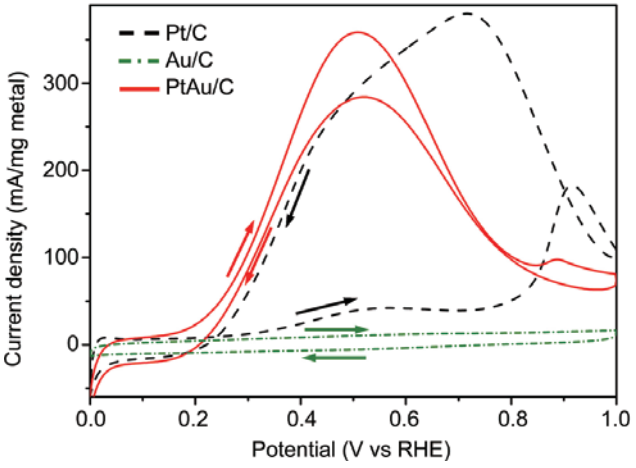


**Figure 5** Cyclic voltammetry of formic acid oxidation catalyzed by carbon-supported PtAu heteronanostructures, Pt nanoparticles and Au nanoparticles. All experiments were conducted in a 0.5 mol/L aqueous solution of formic acid with 0.5 mol/L $H_2SO_4$ as the supporting electrolyte

For bimetallic PtAu/C catalysts, the peak current density reached 359 mA/mg PtAu at around 0.55 V, substantially higher than the value of 43 mA/mg Pt observed for Pt/C catalysts (Fig. 5). The specific activity based on surface area should be even higher for the PtAu/C catalyst, considering the average size of the PtAu alloy nanoparticles was larger than that of the Pt nanoparticles used as the reference. It seems that when platinum was used as the catalyst, both dehydrogenation and dehydration occurred in the oxidation of formic acid. The dehydrogenation occurred in the low potential range, while the dehydration became dominant in the high potential range resulting in a dramatic increase in the surface coverage by adsorbed CO intermediates. When potential was about 0.9 V, the adsorbed $CO_{ads}$ began to be oxidized. The observed high current density in the reverse sweep can be associated with direct formic acid oxidation after the removal of $CO_{ads}$ species [18, 20, 21]. As a comparison, carbon-supported pure Au nanoparticles show no activity toward the oxidation of formic acid (Fig. 5). The mass current density associated with the oxidation of $CO_{ads}$ species, which is centered around 0.9 V, was much smaller for bimetallic PtAu/C catalysts than that for the Pt/C catalyst. The ratio between these two peak current densities ($I_{0.9}/I_{0.55}$) in the positive scan decreased from 4.2 for Pt/C to 0.28 to PtAu/C. This result indicates that the dehydrogenation reaction was preferred on the Pt-rich surfaces of PtAu alloy heteronanostructures. Changes in surface electronic structure could be a factor in the much improved activity in this bimetallic system, as density function theory (DFT) calculations have shown [31–33] that the d-band center shifts from −2.25 eV for platinum to around −1.80 eV for either PtAu alloys or Pt overlayers on Au. Interestingly, the d-band center for PtAu alloy is similar to that for pure Pd metal (−1.83 eV), which catalyzes the oxidation of formic acid predominantly via the dehydrogenation pathway [51, 52].

CO stripping was used to study the shift in d-band center, as the affinity of CO molecules on Pt sites can be directly correlated to the change of peak positions due to the oxidation when the potential is above 0.60 V (Fig. 6). For pure Pt catalysts, the current density for this oxidation peaked at 0.73 V. The absorbed CO could be completely removed from the surface during the first cycle, judging by the disappearance of this signature peak and the subsequent appearance of hydrogen adsorption/desorption peaks. The onset potential for PtAu/C catalysts however shifted positively by more than 100 mV during the first sweep. A peak centered at 0.84 V was readily detectable but diminished over cycles. These observations indicate that the interactions between CO and the active sites on the PtAu surface were stronger than that for pure Pt, which could be attributed to an up-shift in Pt d-band center due to the incorporation of Au.

The accumulation of $CO_{ads}$ species on a surface generally leads to reduced activities over time [26, 53]. Figure 7 shows the activities of carbon-supported PtAu and pure Pt catalysts after multiple CV cycles. The PtAu catalyst had a much higher mass current density than Pt at both 0.3 and 0.5 V during both the initial and subsequent cycles, demonstrating the superior performance of alloy catalyst. Overall, the mass current density for PtAu catalysts decreased only slightly and stabilized over cycles, suggesting the majority of $CO_{ads}$ species can be removed via potential cycling. Besides the electronic factor, incorporation of Au atoms on the surface helps in suppressing the dehydration pathway, which requires the presence of neighboring Pt sites for both generation and oxidation of CO-like intermediates [54, 55]. The modification in electronic and geometric structures of surface platinum

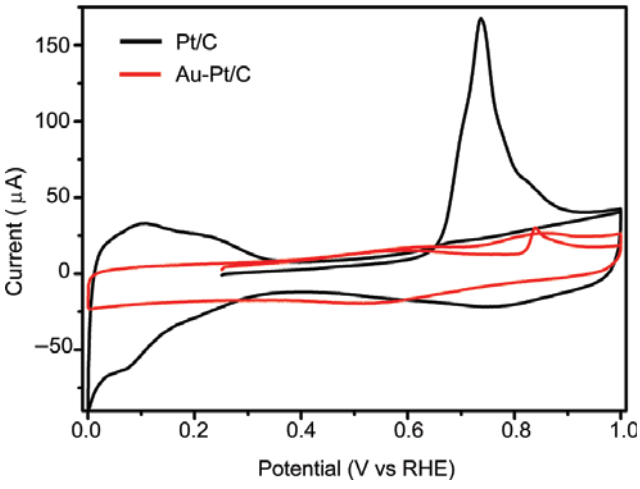


**Figure 6** CV curves of CO stripping on the surfaces of carbon-supported Pt (60 wt% Pt) and PtAu bimetallic nanostructures. All tests were conducted in 0.1 mol/L aqueous solutions of $HClO_4$ under argon protection

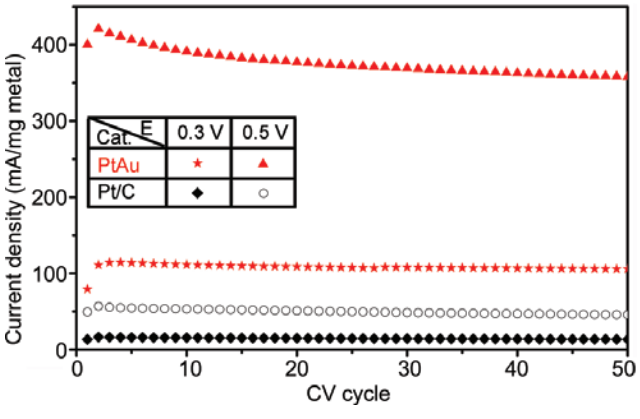


**Figure 7** Change of current density over CV cycles at 0.3 and 0.5 V for carbon-supported PtAu heteronanostructures and Pt nanoparticles. All experiments were conducted in a 0.5 mol/L aqueous solution of formic acid using 0.5 mol/L $H_2SO_4$ as the supporting electrolyte

due to the formation of bimetallic PtAu are probably the main reasons for the observed enhancement in catalytic activities.

## 3. Conclusions

Despite the lack of miscibility between Pt and Au metals in bulk materials at low temperature, Pt-surface rich PtAu bimetallic heteronanostructures can be produced from Pt-on-Au nanoparticles made from molecular precursors. Carbon-supported PtAu bimetallic catalysts exhibit much higher electrocatalytic activity than Pt in the oxidation of formic acid, partially because Pt-rich PtAu alloy surfaces have electronic configurations that favor the dehydrogenation pathway and geometric structures that help to reduce CO poisoning. The conversion from particle-on-particle to Pt-surface rich bimetallic heteronanostructures can be very useful in the design and preparation of multifunctional nanoalloys.

## Acknowledgements

This work was supported by U.S. National Science Foundation (DMR-0449849). It made use of Shared Experimental Facilities at the University of Rochester River Campus Electron Microscope Lab and at the Cornell Center for Materials Research (CCMR) supported by NSF. We thank Mr. Hongjun You for help.

**Electronic Supplementary Material:** Four figures showing the EDX spectrum of Pt-on-Au nanoparticles, TEM images of Pt-on-Au nanoparticles, TEM images of commercial carbon-supported Pt and Au catalysts, and cylic voltammetry curves of commercial carbon-supported Pt and Au catalysts and PtAu bimetallic nanostructures are available in the online version of this article at http://dx.doi.org/10.1007/s12274-009-9040-9 and are accessible free of charge.

## References

[1] Peng, Z. M.; Yang, H. Designer platinum nanoparticles: Control of shape, composition in alloy, nanostructure and electrocatalytic property. *Nano Today* **2009,** *4,* 143–164.

[2] Zhang, J. L.; Sasaki, K.; Sutter, E.; Adzic, R. R. Stabilization of platinum oxygen-reduction electrocatalysts using gold clusters. *Science* **2007,** *315,* 220–222.

[3] Stamenkovic, V. R.; Mun, B. S.; Arenz, M.; Mayrhofer, K. J. J.; Lucas, C. A.; Wang, G. F.; Ross, P. N.; Markovic, N. M. Trends in electrocatalysis on extended and nanoscale Pt-bimetallic alloy surfaces. *Nat. Mater.* **2007,** *6,* 241–247.

[4] Stamenkovic, V. R.; Fowler, B.; Mun, B. S.; Wang, G. F.; Ross, P. N.; Lucas, C. A.; Markovic, N. M. Improved oxygen reduction activity on $Pt_3Ni(111)$ via increased surface site availability. *Science* **2007,** *315,* 493–497.

[5] Park, I. S.; Lee, K. S.; Choi, J. H.; Park, H. Y.; Sung, Y. E. Surface structure of Pt-modified Au nanoparticles and electrocatalytic activity in formic acid electro-oxidation. *J.*

*Phys. Chem. C* **2007,** *111,* 19126–19133.

[6] Habas, S. E.; Lee, H.; Radmilovic, V.; Somorjai, G. A.; Yang, P. Shaping binary metal nanocrystals through epitaxial seeded growth. *Nat. Mater.* **2007,** *6,* 692–697.

[7] Gasteiger, H. A.; Kocha, S. S.; Sompalli, B.; Wagner, F. T. Activity benchmarks and requirements for Pt, Pt-alloy, and non-Pt oxygen reduction catalysts for PEMFCs. *Appl. Catal. B-Environ.* **2005,** *56,* 9–35.

[8] Burda, C.; Chen, X. B.; Narayanan, R.; El-Sayed, M. A. Chemistry and properties of nanocrystals of different shapes. *Chem. Rev.* **2005,** *105,* 1025–1102.

[9] Rodriguez, J. A.; Goodman, D. W. The nature of the metal–metal bond in bimetallic surfaces. *Science* **1992,** *257,* 897–903.

[10] Stamenkovic, V. R.; Mun, B. S.; Mayrhofer, K. J. J.; Ross, P. N.; Markovic, N. M. Effect of surface composition on electronic structure, stability, and electrocatalytic properties of Pt-transition metal alloys: Pt-skin versus Pt-skeleton surfaces. *J. Am. Chem. Soc.* **2006,** *128,* 8813–8819.

[11] Tao, F.; Grass, M. E.; Zhang, Y. W.; Butcher, D. R.; Renzas, J. R.; Liu, Z.; Chung, J. Y.; Mun, B. S.; Salmeron, M.; Somorjai, G. A. Reaction-driven restructuring of Rh–Pd and Pt–Pd core-shell nanoparticles. *Science* **2008,** *322,* 932–934.

[12] Koh, S.; Strasser, P. Electrocatalysis on bimetallic surfaces: Modifying catalytic reactivity for oxygen reduction by voltammetric surface dealloying. *J. Am. Chem. Soc.* **2007,** *129,* 12624–12625.

[13] Teng, X. W.; Black, D.; Watkins, N. J.; Gao, Y. L.; Yang, H. Platinum–maghemite core-shell nanoparticles using a sequential synthesis. *Nano Lett.* **2003,** *3,* 261–264.

[14] Teng, X. W.; Yang, H. Synthesis of magnetic nanocomposites and alloys from platinum-iron oxide core-shell nanoparticles. *Nanotechnology* **2005,** *16,* S554–S561.

[15] Kashchiev, *D. Nucleation: Basic Theory with Applications*; Butterworth Heinemann: Oxford, 2000.

[16] Zhang, J. L.; Vukmirovic, M. B.; Xu, Y.; Mavrikakis, M.; Adzic, R. R. Controlling the catalytic activity of platinum-monolayer electrocatalysts for oxygen reduction with different substrates. *Angew. Chem. Int. Edit.* **2005,** *44,* 2132–2135.

[17] Adzic, R. R.; Zhang, J. L.; Sasaki, K.; Vukmirovic, M. B.; Shao, M.; Wang, J. X.; Nilekar, A. U.; Mavrikakis, M.; Valerio, J. A.; Uribe, F. Platinum monolayer fuel cell electrocatalysts. *Top. Catal.* **2007,** *46,* 249–262.

[18] Markovic, N. M.; Gasteiger, H. A.; Ross, P. N.; Jiang, X. D.; Villegas, I.; Weaver, M. J. Electrooxidation mechanisms of methanol and formic-acid on Pt–Ru alloy surfaces. *Electrochim. Acta* **1995,** *40,* 91–98.

[19] Rice, C.; Ha, R. I.; Masel, R. I.; Waszczuk, P.; Wieckowski, A.; Barnard, T. Direct formic acid fuel cells. *J. Power Sources* **2002,** *111,* 83–89.

[20] Chen, Y. X.; Heinen, M.; Jusys, Z.; Behm, R. B. Kinetics and mechanism of the electrooxidation of formic acid—Spectroelectrochemical studies in a flow cell. *Angew. Chem. Int. Edit.* **2006,** *45,* 981–985.

[21] Lovic, J. D.; Tripkovic, A. V.; Gojkovic, S. L. J.; Popovic, K. D.; Tripkovic, D. V.; Olszewski, P.; Kowal, A. Kinetic study of formic acid oxidation on carbon-supported platinum electrocatalyst. *J. Electroanal. Chem.* **2005,** *581,* 294–302.

[22] Zhu, Y. M.; Ha, S. Y.; Masel, R. I. High power density direct formic acid fuel cells. *J. Power Sources* **2004,** *130,* 8–14.

[23] Rice, C.; Ha, S.; Masel, R. I.; Wieckowski, A. Catalysts for direct formic acid fuel cells. *J. Power Sources* **2003,** *115,* 229–235.

[24] Jeong, K. J.; Miesse, C. A.; Choi, J. H.; Lee, J.; Han, J.; Yoon, S. P.; Nam, S. W.; Lim, T. H.; Lee, T. G. Fuel crossover in direct formic acid fuel cells. *J. Power Sources* **2007,** *168,* 119–125.

[25] Choi, J. H.; Jeong, K. J.; Dong, Y.; Han, J.; Lim, T. H.; Lee, J. S.; Sung, Y. E. Electro-oxidation of methanol and formic acid on PtRu and PtAu for direct liquid fuel cells. *J. Power Sources* **2006,** *163,* 71–75.

[26] Capon, A.; Parsons, R. Oxidation of formic-acid at noble-metal electrodes: Part 3. Intermediates and mechanism on platinum-electrodes. *J. Electroanal. Chem.* **1973,** *45,* 205–231.

[27] Matsumoto, F.; Roychowdhury, C.; DiSalvo, F. J.; Abruna, H. D. Electrocatalytic activity of ordered intermetallic PtPb nanoparticles prepared by borohydride reduction toward formic acid oxidation. *J. Electrochem. Soc.* **2008,** *155,* B148–B154.

[28] Alden, L. R.; Han, D. K.; Matsumoto, F.; Abruna, H. D.; DiSalvo, F. J. Intermetallic PtPb nanoparticles prepared by sodium naphthalide reduction of metal-organic precursors: Electrocatalytic oxidation of formic acid. *Chem. Mater.* **2006,** *18,* 5591–5596.

[29] Roychowdhury, C.; Matsumoto, F.; Zeldovich, V. B.; Warren, S. C.; Mutolo, P. F.; Ballesteros, M.; Wiesner, U.; Abruna, H. D.; DiSalvo, F. J. Synthesis, characterization, and electrocatalytic activity of PtBi and PtPb nanoparticles prepared by borohydride reduction in methanol. *Chem.*

*Mater.* **2006,** *18,* 3365–3372.

[30] Casado-Rivera, E.; Volpe, D. J.; Alden, L.; Lind, C.; Downie, C.; Vazquez-Alvarez, T.; Angelo, A. C. D.; DiSalvo, F. J.; Abruna, H. D. Electrocatalytic activity of ordered intermetallic phases for fuel cell applications. *J. Am. Chem. Soc.* **2004,** *126,* 4043–4049.

[31] Greeley, J.; Norskov, J. K.; Mavrikakis, M. Electronic structure and catalysis on metal surfaces. *Annu. Rev. Phys. Chem.* **2002,** *53,* 319–348.

[32] Hammer, B.; Norskov, J. K. Theoretical surface science and catalysis—Calculations and concepts. *Adv. Catal.* **2000,** *45,* 71–129.

[33] Ruban, A.; Hammer, B.; Stoltze, P.; Skriver, H. L.; Norskov, J. K. Surface electronic structure and reactivity of transition and noble metals. *J. Mol. Catal. A-Chem.* **1997,** *115,* 421–429.

[34] Lee, J. K.; Lee, J.; Han, J.; Lim, T. H.; Sung, Y. E.; Tak, Y. Influence of Au contents of AuPt anode catalyst on the performance of direct formic acid fuel cell. *Electrochim. Acta* **2008,** *53,* 3474–3478.

[35] Kristian, N.; Yan, Y. S.; Wang, X. Highly efficient submonolayer Pt-decorated Au nano-catalysts for formic acid oxidation. *Chem. Commun.* **2008,** 353–355.

[36] Kim, J.; Jung, C.; Rhee, C. K.; Lim, T. H. Electrocatalytic oxidation of formic acid and methanol on Pt deposits on Au(111). *Langmuir* **2007,** *23,* 10831–10836.

[37] Duan, H. W.; Nie, S. M. Etching colloidal gold nanocrystals with hyperbranched and multivalent polymers: A new route to fluorescent and water-soluble atomic clusters. *J. Am. Chem. Soc.* **2007,** *129,* 2412–2413.

[38] Brust, M.; Walker, M.; Bethell, D.; Schiffrin, D. J.; Whyman, R. Synthesis of thiol-derivatized gold nanoparticles in a 2-phase liquid-liquid system. *J. Chem. Soc. Chem. Commun.* **1994,** 801–802.

[39] Bauer, E.; Vandermerwe, J. H. Structure and growth of crystalline superlattices—From monolayer to superlattice. *Phys. Rev. B* **1986,** *33,* 3657–3671.

[40] Porter, D. A.; Easterling, K. E. *Phase Transformation in Metals and Alloys*; Chapman & Hall: London, 1992.

[41] Chambers, S. A. Epitaxial growth and properties of thin film oxides. *Surf. Sci. Rep.* **2000,** *39,* 105–180.

[42] Ji, X. H.; Song, X. N.; Li, J.; Bai, Y. B.; Yang, W. S.; Peng, X. G. Size control of gold nanocrystals in citrate reduction: The third role of citrate. *J. Am. Chem. Soc.* **2007,** *129,* 13939–13948.

[43] Hu, M.; Chen, J. Y.; Li, Z. Y.; Au, L.; Hartland, G. V.; Li, X. D.; Marquez, M.; Xia, Y. N. Gold nanostructures: Engineering their plasmonic properties for biomedical applications. *Chem. Soc. Rev.* **2006,** *35,* 1084–1094.

[44] Xia, Y. N.; Halas, N. J. Shape-controlled synthesis and surface plasmonic properties of metallic nanostructures. *MRS Bull.* **2005,** *30,* 338–344.

[45] Vegard, L.; Dale, H. Untersuchungen ueber Mischkristalle und Legierungen. *Zeits. Krist.* **1928,** *67,* 148–162.

[46] Peng, Z. M.; Yang, H. Ag–Pt alloy nanoparticles with the compositions in the miscibility gap. *J. Solid State Chem.* **2008,** *181,* 1546–1551.

[47] Xu, J. B.; Zhao, T. S.; Liang, Z. X. Synthesis of active platinum–silver alloy electrocatalyst toward the formic acid oxidation reaction. *J. Phys. Chem. C* **2008,** *112,* 17362–17367.

[48] Adhikari, H.; Marshall, A. F.; Goldthorpe, I. A.; Chidsey, C. E. D.; McIntyre, P. C. Metastability of Au–Ge liquid nanocatalysts: Ge vapor–liquid–solid nanowire growth far below the bulk eutectic temperature. *ACS Nano* **2007,** *1,* 415–422.

[49] Luo, J.; Wang, L. Y.; Mott, D.; Njoki, P. N.; Lin, Y.; He, T.; Xu, Z. C.; Wanjana, B. N.; Lim, I. S.; Zhong, C. J. Core/shell nanoparticles as electrocatalysts for fuel cell reactions. *Adv. Mater.* **2008,** *20,* 4342–4347.

[50] Zhao, D.; Xu, B. Q. Platinum covering of gold nanoparticles for utilization enhancement of Pt in electrocatalysts. *Phys. Chem. Chem. Phys.* **2006,** *8,* 5106–5114.

[51] Zhou, W. P.; Lewera, A.; Larsen, R.; Masel, R. I.; Bagus, P. S.; Wieckowski, A. Size effects in electronic and catalytic properties of unsupported palladium nanoparticles in electrooxidation of formic acid. *J. Phys. Chem. B* **2006,** *110,* 13393–13398.

[52] Hoshi, N.; Kida, K.; Nakamura, M.; Nakada, M.; Osada, K. Structural effects of electrochemical oxidation of formic acid on single crystal electrodes of palladium. *J. Phys. Chem. B* **2006,** *110,* 12480–12484.

[53] Jiang, J.; Kucernak, A. Nanostructured platinum as an electrocatalyst for the electrooxidation of formic acid. *J. Electroanal. Chem.* **2002,** *520,* 64–70.

[54] Kristian, N.; Yan, Y. S.; Wang, X. Highly efficient submonolayer Pt-decorated Au nano-catalysts for formic acid oxidation. *Chem. Commun.* **2008,** 353–355.

[55] Neurock, M.; Janik, M.; Wieckowski, A. A first principles comparison of the mechanism and site requirements for the electrocatalytic oxidation of methanol and formic acid over Pt. *Faraday Discuss.* **2008,** *140,* 363–378.